Article scientifique   Article   2020   Accepted version   Open Access

This is an author manuscript post-peer-reviewing (accepted version) of the original publication. The layout of the published version may differ .

- -

Multiorder Nonlinear Mixing in Metal Oxide Nanoparticles

- -

Campargue, Gabriel; La Volpe, Luca; Giardina, Gabriel; Gaulier, Geoffrey; Lucarini, Fiorella; Gautschi, Ivan; Le Dantec, Ronan; Staedler, Davide; Diviani, Dario; Mugnier, Yannick; Wolf, Jean-Pierre; Bonacina, Luigi

This publication URL: https://archive-ouverte.unige.ch//unige:145483
Publication DOI: 10.1021/acs.nanolett.0c03559

Multi-order Nonlinear Mixing in Metal Oxide Nanoparticles

Gabriel Campargue,[†] Luca La Volpe,[†] Gabriel Giardina,[†] Geoffrey Gaulier,[†] Fiorella

Lucarini,[‡] Ivan Gautschi,[‡] Ronan Le Dantec,[¶] Davide Staedler,[‡] Dario Diviani,[‡]

Yannick Mugnier,[¶] Jean-Pierre Wolf,[†] and Luigi Bonacina[*,†]

†*Department of Applied Physics, Université de Genève, 22 chemin de Pinchat, 1211*
Genève 4, Switzerland

‡*Université de Lausanne, Faculty of Biology and Medicine, Department of Biomedical*
Sciences

¶*Univ. Savoie Mont Blanc, SYMME, F-74000 Annecy, France*

E-mail: gabriel.campargue@unige.ch

Abstract

While most of the reports on the nonlinear properties of micro- and nano-structures address the generation of distinct signals, such as second or third harmonic, here we demonstrate that the novel generation of dual output lasers recently developed for microscopy can readily increase the accessible parameter space and enable the simultaneous excitation and detection of multiple emission orders such as several harmonics and signals stemming from various sum and difference frequency mixing processes. This rich response, which, in our case, features ten distinct emissions and encompasses the whole spectral range from the deep ultraviolet to the short-wave infrared region, is demonstrated using various nonlinear oxide nanomaterials while being characterized

and simulated temporally and spectrally. Notably, we show that the response is conserved when the particles are embedded in biological media opening the way to novel biolabelling and photo-triggering strategies.

Keywords

Dielectric Nanoparticles, Metal Oxides, Nonlinear Microscopy, Harmonic Generation, Frequency Mixing, Ultrafast Optics

Introduction

Within the perturbative approach of nonlinear optics, no more than the few lowest orders of the susceptibility development ($\chi^{(n)}$ with $n \leq 5$) can engender a large manifold of parametric interactions. However, the comprehensive investigation of this extremely rich and multi-faceted response has been so far hindered by the use of phase-matched crystals, which provide sizeable signals only at selected frequencies.[1] Likewise, spectral broadening by Self-Phase-Modulation (SPM)[2] might hamper the detection of these signals. Nowadays, the combination of tunable ultrafast high repetition rate laser sources with sub-wavelength dielectric structures is disclosing a largely unexplored territory. The research focus has been so far set on nano-engineering dielectric substrates to exploit specific resonance modes, with the major goal of embedding micrometric frequency-mixers in optoelectronic components.[3–5] In this work, we show that metal oxide nanoparticles of various chemical compositions (harmonic nanoparticles, HNPs) and with no prior morphology- or size-selection can readily generate multiple signals spanning from the deep ultraviolet (DUV) to the shortwave infrared (SWIR) region. Their optical response includes various harmonic orders, and, upon two-color excitation, several frequency-sum and difference combinations. Some of these signals exerted on micro- and nano-structures have been previously observed individually[6–8] or in combinations of two or three of them.[9–15] Very recently, Liu *et al.* reported the simultaneous emission of

harmonics and wave-mixing signals from a 3 μm diameter region of a GaAs-based dielectric metasurface optimized for 1.24 and 1.57 μm excitation using a kHz source.[16] Here, using a dual output laser developed for microscopy and sub-micron particles, we demonstrate a similar multi-order phase-coherent response spanning from fifth harmonic generation (FiHG) of a 1300 nm pulse (260 nm) to four-wave mixing (4WM) leading to emission at 2061 nm. Notably, the response is conserved when the particles are embedded in biological media and under laser-scanning conditions accessible thanks to the MHz repetition rate of the source, which opens the way to bio-imaging and photo-interaction schemes.

Results

In Fig. 1, we present the multi-order response detected from a $KNbO_3$ HNP, upon two-color excitation at 1045 and 1300 nm resolved spectrally from DUV (260 nm) to NIR (874 nm) (horizontal axis) and as a function of the delay Δt between the two excitation pulses (vertical axis). The peak intensity at the focus is 5.5 and 1.7 TW/cm^2 for the 1045 and 1300 nm excitation, respectively. Details on the experimental set-up together with the protocols for sample preparation are provided in sections S.I. 1 and 2. In S.I. 3, we describe the procedure followed to compose the dataset in Fig. 1. Note that, differently from previous reports,[17–19] here we did not apply specific protocols to ensure to have a single nanocrystal in the focus of the objective (*e.g.*, correlation with electron/atomic force microscopy, polarization analysis). Therefore, although we systematically searched for objects smaller than the point spread function of the set-up, we cannot exclude the presence of small aggregates instead of isolated nanoparticles (see Fig. S.I. 2 and S.I. 3).

In the image, the mechanism leading to each emission is reported as a combination of upwards and downwards arrows, indicating the addition or the subtraction of a photon from the 1045 nm (light brown) and 1300 nm (black) laser beam. Direct harmonic signals, such as second harmonic generation (SHG) at 522 and 650 nm, or third harmonic generation (THG)
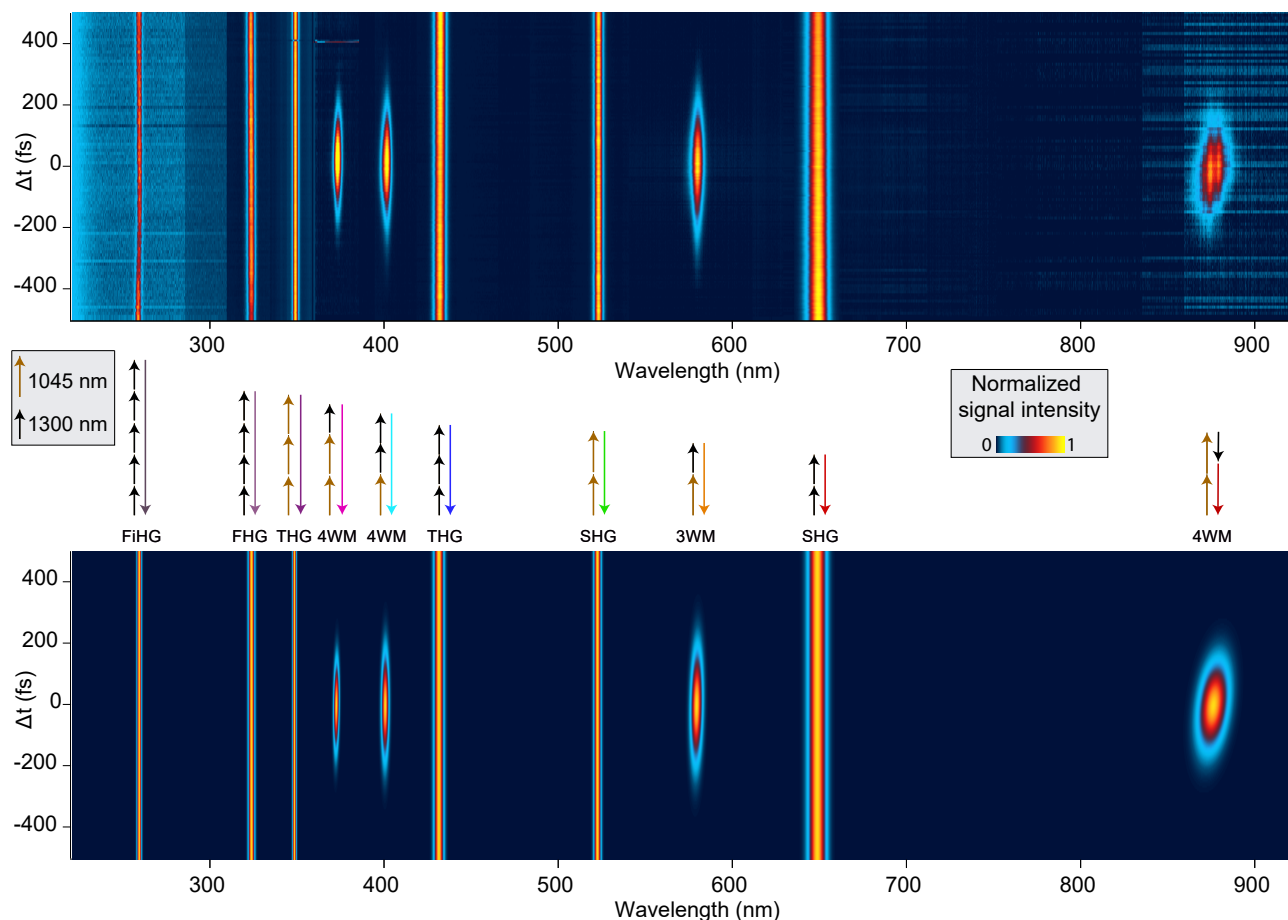
Figure 1: *Top:* Intensity-normalized spectrograms obtained from a sub-diffraction limited KNbO$_3$ HNP upon simultaneous 1300 and 1045 nm excitation. Direct harmonic signals (SHG, THG, FHG, FiHG) appear as continuous vertical stripes as they do not depend on the relative pulse delay Δt, contrary to signals generated by the superposition of the 1300 and 1045 nm pulses (3WM and 4WM) which display a clear Δt dependence. Note the absence of supercontinuum background and luminescence in the response. *Center:* Photon-combinations leading to each distinct spectral element of the response. *Bottom:* Simulated spectrograms.

at 348 and 433 nm, appear as continuous vertical stripes as they do not depend on the relative pulse delay, Δt.

The spectrogram at 579 nm, obtained by 1045 and 1300 nm sum frequency mixing, corresponds to the well-known Cross Frequency Resolved Optical Gating (XFROG)[20] of the two excitation pulses and its duration is determined by the cross-convolution of their temporal envelopes.[21] The complete response from the KNbO$_3$ particle includes two harmonics generated by the 1045 nm beam (523 and 348 nm) and four by the 1300 nm (650, 433, 325 and

260 nm), frequency sums involving three-wave mixing (3WM, 586 nm) and four-wave mixing (373 and 401 nm) processes, associated with $\chi^{(2)}$ and $\chi^{(3)}$, respectively, and, finally, a 4WM, involving a negative wave contribution, leading to 874 nm emission. We were not able to detect the fourth harmonic (FHG) of the 1045 nm pulse, which should lie very close to the fifth harmonic (FiHG) of the 1300 nm pulse.

Within our experimental sensitivity, we did not observe any time-dependent intensity variation of the traces associated with the $\chi^{(2)}$ response, which could have been assigned to multi-step generation (see section S.I. 5). Similarly, we do not report any intensity decrease with picosecond-time recovery, such as those that Liu *et al.* attributed to the recombination of pump-generated free-carriers in a GaAs metasurface.[16] We also do not observe supercontinuum generation by SPM nor, consistently with previous assessments, fluorescence from the particles. In general, we highlight the high photostability of the $KNbO_3$ sample. For a reference, the acquisition of each spectral slice (as delimited by the vertical dashed lines in Fig. S.I. 4) took between 30 seconds and 5 minutes depending on signal intensity (the longest acquisitions apply to FHG and FiHG). All spectrograms were sequentially performed on the same object. On the other hand, other materials tested, such as $BiFeO_3$, display a markedly lower photo-stability when excited at wavelengths ≤ 980 nm as previously reported.[22]

The assignments of the temporal and spectral features observed are in line with the simulated response presented in the lower panel of Fig. 1. The traces were analytically calculated assuming Gaussian temporal and spectral profiles for the two fundamental pulses and neglecting phase-matching effects, in agreement with the sub-coherence length dimensions of the emitters. The spectral widths were set to the experimental values (9.35 nm at 1045 nm, and 16.96 nm at 1300 nm). For the temporal component, we calculated the Fourier-transform duration from the laser spectra and assumed exclusively second-order phase-distortions (*i.e.*, linear chirp) described by the quadratic phase parameter ϕ adjusted to yield the largest overlap with the experimental spectrograms in the wavelength/Δt space (see section S.I. 4). Note that the model we devised did not include field confinement effects, Mie resonances[23,24]

nor absorption or refraction by the particles or the optical elements in the set-up. The best agreement was found for the quadratic phase values -5053 fs^2 and -2250 fs^2 for the fixed and tunable output, leading to pulse duration at the focus of 190 fs and 153 fs, respectively. Incidentally, we remark that negative delay dispersion is consistent with the large precompensation values of the laser set by the manufacturer, which is designed to be coupled with microscope systems containing more transmissive optical components than our custom set-up. Indeed, we systematically observed that working at the lower edge of the precompressor unit of the tunable output yielded the highest nonlinear conversion.

Being ω_1 and ω_2 the carrier frequencies of the two laser outputs and n_1 and $n_2 \in \mathbb{Z}$ their weight in the non-linear combination, the temporal duration of the ith non-linear emission, centred at the frequency $\omega_i = n_1\omega_1 + n_2\omega_2$, can be readily calculated as

$$\tau_i = \left(\frac{|n_1|}{\tau_{1c}^2} + \frac{|n_2|}{\tau_{2c}^2} \right)^{-\frac{1}{2}} \tag{1}$$

where τ_{1c} and τ_{2c} are the temporal duration of the input pulses, which depends on their chirp, $\tau_c = \tau\sqrt{1 + \frac{\phi^2}{4\tau^4}}$ with τ being their Fourier-transform-limited duration and ϕ the quadratic phase. The pulse duration of each non-linear emission is therefore modulated by the weight of each input pulse in the nonlinear combinations. For example, the calculated duration of the two 4WM presented in Fig. 1 at 373 nm and 401 nm are 101 fs and 94 fs, respectively. These durations should not be confused with the different temporal spread of the 3WM and 4WM spectrograms in Fig.1, which are function of the time delay Δt between the two input pulses. More examples can be found in Fig. S.I. 5.

The frequency mixing schemes one can apply are not limited to the spectral range covered by Fig. 1. In fact, as reported in Fig. 2, by choosing a different wavelength for the tunable output (780 nm instead of 1300 nm), the same sub-diffraction limited KNbO$_3$ HNP emits also in the short-wave infrared region (SWIR, 1-2.5 µm) at 1583 nm (green trace) by the
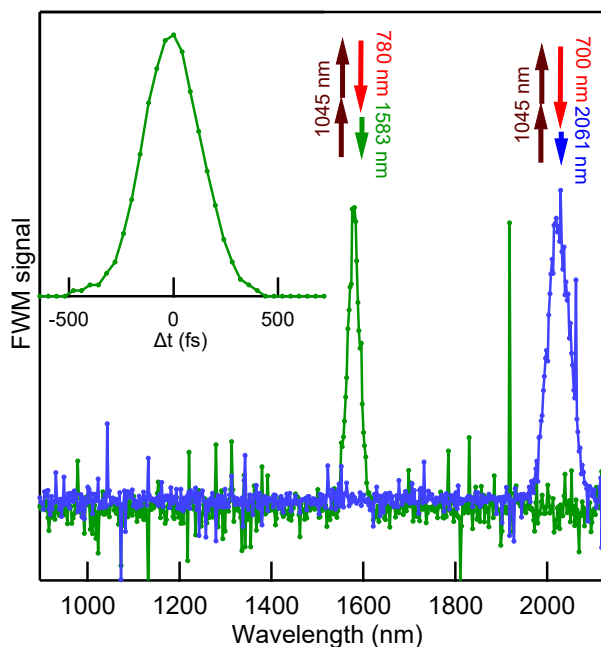
Figure 2: SWIR emission by a diffraction limited KNbO$_3$ HNP upon two-color excitation. *Green trace*: 4WM spectrum at zero time-delay centered at 1583 nm upon 780 and 1045 nm excitation. *Inset*: corresponding temporal cross correlation. *Blue trace*: 4WM spectrum at 2061 nm upon 700 and 1045 nm excitation.

following 4WM process:

$$\lambda_{4WM} = \frac{1}{\frac{2}{\lambda_1} - \frac{1}{\lambda_2}}$$
$$= \frac{1}{\frac{2}{1045\,\text{nm}} - \frac{1}{780\,\text{nm}}} = 1583\,\text{nm} \tag{2}$$

In the inset, we report the corresponding temporal cross-correlation. This specific wavelength combination was chosen to generate an exemplary signal in the telecom range. By tuning the laser output to 700 nm, we produced an emission at 2061 nm (blue trace), at the long-wavelength detection edge of our set-up.

A critical aspect to carefully consider (in particular in view of applications) concerns the relative intensities of the emission peaks. The yellow traces in Fig. 3 indicate that for KNbO$_3$ the peak maxima span several orders of magnitude for a given set of excitation pulse inten-

sities. It is known that the nonlinear response of dielectric nanoparticles depends on the interplay of numerous spectral, material, morphological, and polarization-dependent parameters. In Fig. 3, along with $KNbO_3$ (average dynamic light scattering (DLS) size 100 nm, see section S.I. 2), we report also the response of $BiFeO_3$ (green, average DLS size 100 nm), $LiNbO_3$ (red, average DLS size 60 nm), and ZnO particles (blue, average DLS size 140 nm) under similar excitation settings. The signals are expected to increase as the volume squared, as previously shown for $\chi^{(2)}$ processes in noncentrosymmetric oxides larger than 20 nm in SHG microscopy[18] and ensemble measurements.[25] Such volume dependence could explain, for instance, the two orders of magnitude difference for SHG between $LiNbO_3$ and $KNbO_3$. In fact these two materials possess a similar orientation-averaged second-order bulk susceptibility[26] ($\langle\chi^{(2)}\rangle \approx$ 30-35 pm/V) and their diameters determined by DLS differ by a factor two in our experiment. Likewise, the similar SHG and 3WM traces obtained for $KNbO_3$ and ZnO result from a larger nanoparticle size for ZnO since its $\langle\chi^{(2)}\rangle$ is below 6 pm/V.[27,28] Finally, for $BiFeO_3$, the stronger SHG and 3WM traces could be attributed to its higher $\langle\chi^{(2)}\rangle$ of 100 pm/V and the trend of decreasing conversion efficiency for longer excitation wavelength previously observed within the 800-1300 nm range.[25] Nonetheless, the overall spectral responses of Fig. 3 and comparison between nanomaterials are to be considered with great caution. In fact, parametric signals depend on the 3D orientation of the crystallographic axis of the nanoparticles.[17,29] In addition, we cannot exclude that slightly different focusing of the two interacting beams at 1045 nm and 1300 nm play a role in the differences between the SHG and 3WM amplitudes observed for $BiFeO_3$ and $LiNbO_3$. Therefore, it deems extremely complicated to extract reliable information without either i) following an ensemble characterization approach by extending the Hyper Rayleigh Scattering (HRS) formalism to higher nonlinear orders, or ii) proceeding with a bottom up approach concentrating the analysis on emitters well defined in terms of shape, size, and orientation. On the other hand, it is remarkable how under standard excitation and detection conditions and with no particle pre-selection, we are able to easily observe nine nonlinear processes (with the exclusion of
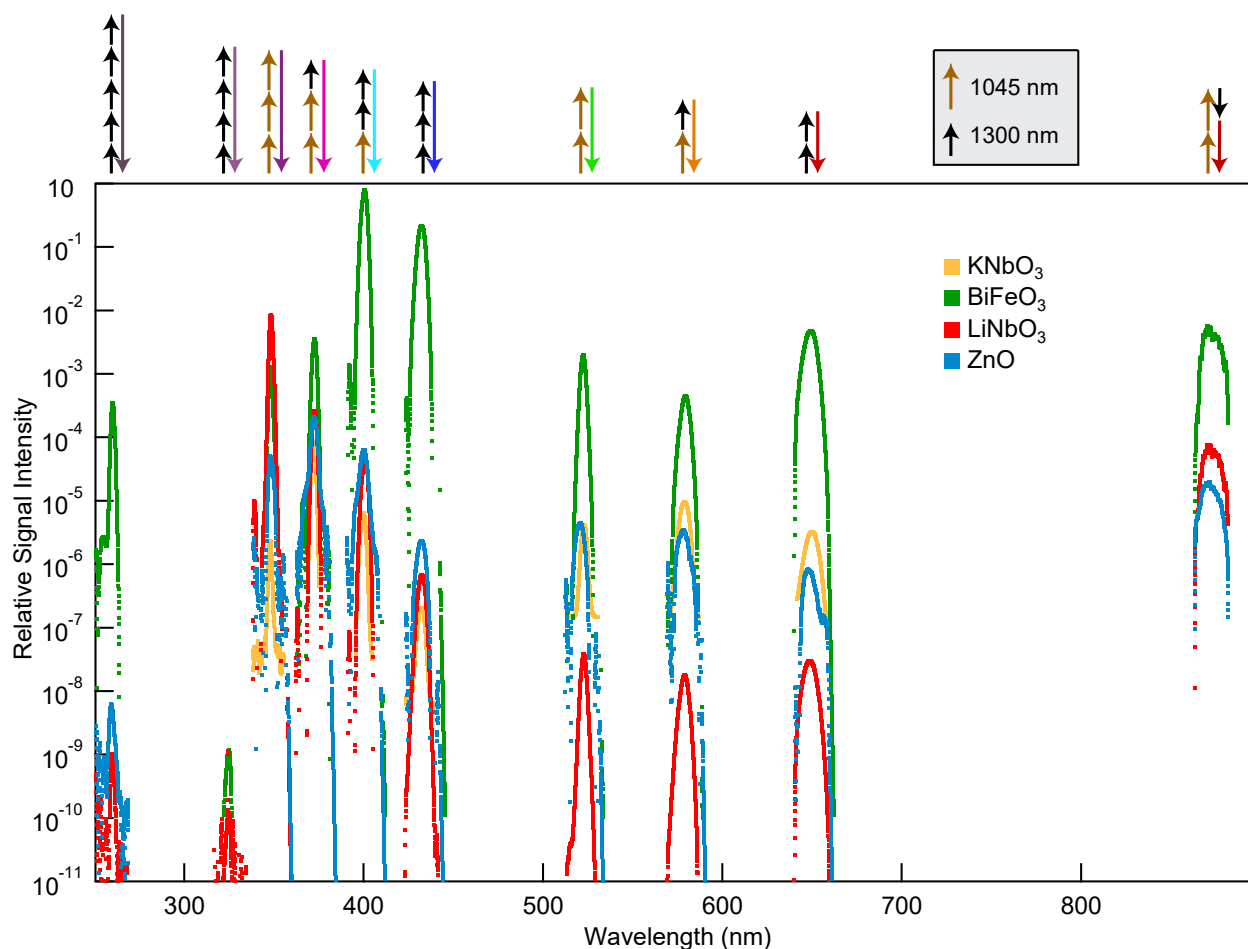
Figure 3: Excitation- and detection-corrected spectral response of HNPs of different metal oxide materials upon 1045 and 1300 nm excitation. The focal intensity corresponds to $1.8\,\mathrm{TW/cm^2}$ for both excitation beams. All traces are normalized to the highest signal obtained ($BiFeO_3$ 4WM at 401 nm).

FHG, which is systematically considerably smaller) from four different HNP materials.

Besides the effect of sample-dependent properties on conversion efficiency, emissions are expected to scale with the excitation intensity according to the order of the nonlinear interaction at their origin. The intensity dependence of the harmonic progression stemming from 1300 nm is reported in the left panel of Fig. 4 up to a maximum intensity of $1\,\mathrm{TW/cm^2}$. The nominal curves (I^n, with $n = 2, 3, 4, 5$) are plotted as continuous lines, the values for the exponent n obtained from fitting the data are reported in parentheses. Ostensibly, the experimental amplitudes are in agreement with the prediction of perturbative nonlinear response throughout the whole range we explored. The perturbative relationship with the excitation

intensity, together with the wavelength and interaction-order flexibility of the approach, is further exemplified by the comparison in the bottom plot of Fig. 4. In this case, we selected two distinct mixing processes leading to emission at 648 nm. This wavelength was obtained on the same $KNbO_3$ object either by 3WM or 4WM , as $\lambda_{3WM} = \frac{1}{\frac{1}{\lambda_1} - \frac{1}{\lambda_2}}$ ($\lambda_1 = 400$ nm ; $\lambda_2 = 1045$ nm) or $\lambda_{4WM} = \frac{1}{\frac{2}{\lambda_1} - \frac{1}{\lambda_2}}$ ($\lambda_1 = 800$ nm; $\lambda_2 = 1045$ nm), respectively. In this comparison, the 1045 nm intensity was kept fixed, while the 400 and 800 nm intensities, which can be read on the horizontal axes labelled I_{400} and I_{800}, were adjusted to yield a similar output at 648 nm. 4WM requires 10 TW/cm^2 800 nm excitation to generate similar signal than 3WM with 0.8 TW/cm^2 400 nm excitation. The dependence on the intensity of the laser at λ_1 scales with the number of photons involved, being linear for I_{400} and quadratic for I_{800}, respectively.

Discussion

Our work highlights the extremely rich optical response that can be obtained by the combination of dual output femtosecond MHz lasers as light sources in scanning microscopy using nonlinear objects as probes. The response observed can be readily associated with processes relying on both the even and the odd orders of the nonlinear susceptibility perturbative development. Although several of these signals have been previously observed separately, the possibility to exert all of them *simultaneously* on sub-micron objects with no pre-selection in terms of size, morphology, and specific chemical composition (here we used 4 different noncentrosymmetric metal oxide nanomaterials) emphasizes the versatility of the approach. In particular, efficient *in situ* frequency conversion can lead to enabling approaches for bio-imaging and for devising novel photo-interaction schemes.[30]

With this kind of applications in mind, we investigated whether the multi-order nonlinear response is preserved when the particles are embedded in a biological environment and not simply dispersed on a substrate in dry form. In the top-left panel of Fig. 5, we present a bright
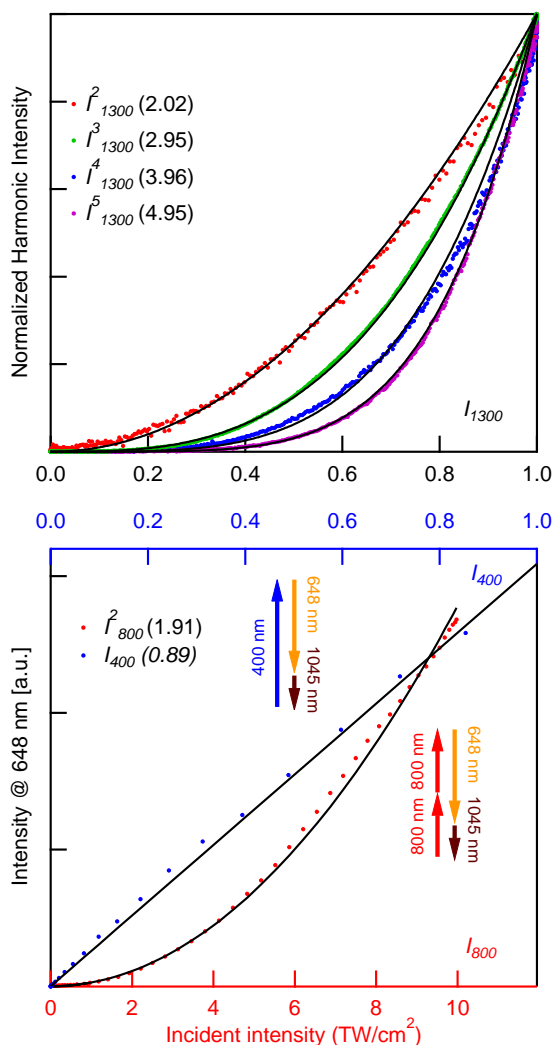
Figure 4: *Top:* Power dependence of the harmonic series obtained from a $BiFeO_3$ HNP upon excitation at 1300 nm. Traces are normalized to their maximum value. Dots: experimental data points. Lines: nominal traces I_{1300}^n, $n = 1, ..., 5$. The values of the exponent n obtained by fitting the function I_{1300}^n to the data points are reported in parantheses. *Bottom:* 648 nm emission from a $KNbO_3$ HNP either by a $\chi^{(2)}$ (400 and 1045 nm excitation, blue) or a $\chi^{(3)}$ (800 and 1045 nm excitation, red) process. The top axis indicates the intensity at 400 nm (I_{400}) and the bottom one at 800 nm (I_{800}), respectively. Dots: experimental data points. Lines: nominal traces I_{400} and I_{800}^2. The values of the exponent n obtained by fitting the function $I_{400,800}^n$ to the data points are reported in parentheses. All horizontal axes report the intensity of the excitation pulses in TW/cm^2.

field microscopy image, where one can distinguish two human cancer cells (DU145 androgen-independent prostate cancer) and numerous $KNbO_3$ HNP aggregates attached to the cell membranes or to the substrate. The corresponding set of multiphoton images acquired by
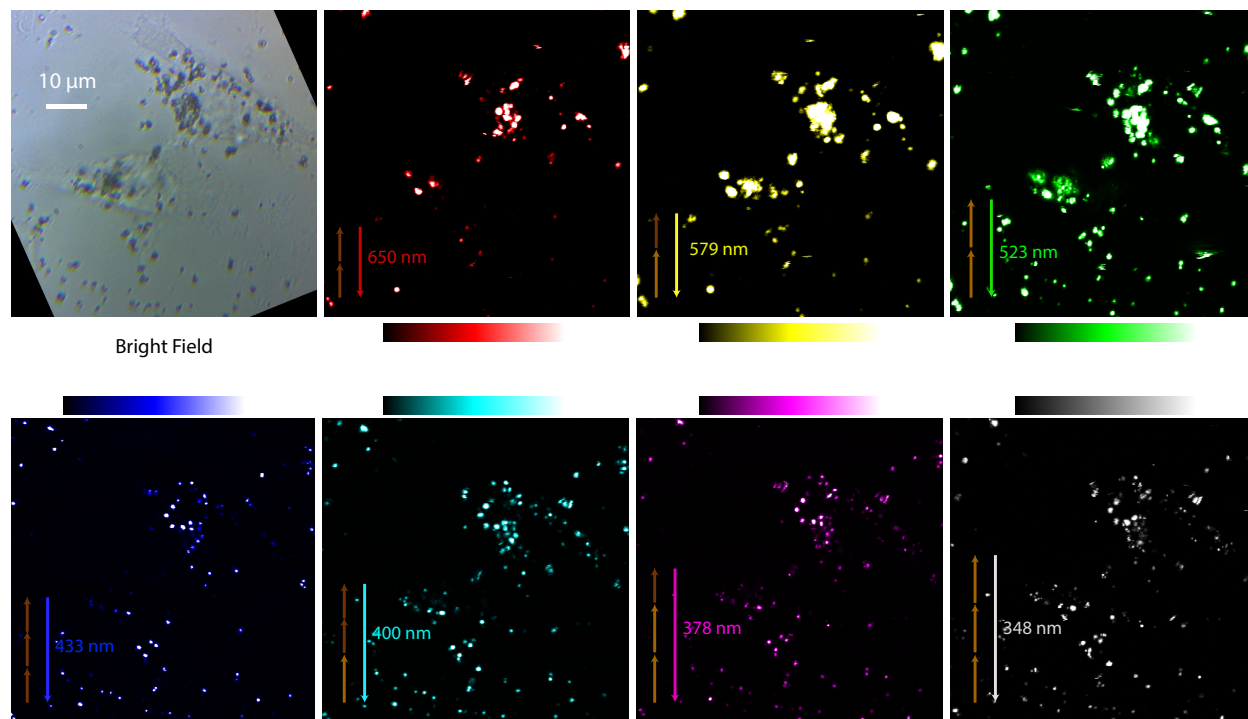
Figure 5: Laser scanning microscopy images of $KNbO_3$ HNPs in contact with human prostate cancer cells upon 1300 and 1045 nm excitation. The 1045 and 1300 nm contribution to the different nonlinear combinations are now plotted as light and dark brown arrows, respectively. *Top panels*: bright field image and 3WM processes (leftmost panel). *Bottom panels*: 4WM processes. The colormap hues are based on the actual wavelengths for visible emissions.

raster-scanning ($60\,\mu s$ dwell time) the 1300 and 1045 nm laser outputs collineraly focused onto the sample through a NA $= 0.75$ air objective is presented in all successive panels. Images are sorted from the longest to the shortest wavelength detected. The panels in the top row correspond to three $\chi^{(2)}$ processes (SHG and 3WM), the ones in the bottom row to four $\chi^{(3)}$ ones (THG and 4WM). Most of the particles are visible in all images, although their relative intensities might vary because of the reasons discussed in the context of Fig. 3 (see also Fig. S.I. 3). The visible improvement in spatial resolution of the $\chi^{(3)}$ series is associated with the higher nonlinearity order, as the effective point spread function (PSF) is the product of the excitation PSFs involved in the interaction.

In previous works, we have shown how the simultaneous detection of SHG and THG from HNPs used as labelling probes for tracking individual cells can greatly improve image-selectivity[14] especially in highly optically congested environments with strong endogenous

sources (collagen and lipids for SHG and THG, respectively).[31] Alternatively, the efficient *in situ* generation of new wavelengths can be used to deploy nonlinear photo-triggering approaches by fully exploiting the nonlinear conversion efficiencies of nanoparticles as opposed to the comparatively smaller nonlinear absorption cross-sections of molecules and drugs.[32,33] The generation of light in the SWIR region, apart from its interest in optoelectronics, can be used in combination with imaging approaches critically requiring low-scattering of the emitted signal for the image formation process, such as nonlinear light-sheet microscopy.[34] Phase-coherent schemes based on two-color interactions have been recently demonstrated for increasing spatial resolution both for scanning[35] and wide-field approaches.[36]

Finally, the analysis of time-resolved traces as reported in Fig. 1 paves the way to refined multi-order pulse characterization methods. In the context of multiphoton microscopy, the use of nanometric objects for femtosecond pulse diagnostics have been already explored bridging to the nanoscale approaches such as SHG autocorrelation and FROG.[37–41] The simultaneous access to multiple nonlinear combinations (and frequencies) demonstrated here can be exploited to avoid temporal ambiguity in the time axis orientation[20] and to gain spectral and temporal resolution due to the higher nonlinearities involved. In Fig S.I. 5, we report a series of simulated spectrograms obtained by changing the ϕ values of the excitation pulses. The shapes of the 3WM and 4WM traces in the Δt/wavelength space change in an non-uniform fashion highlighting the sensitivity to the phase of the two laser outputs. Such an approach could be prospectively used to infer spatially-resolved information about the optical properties of the sample where the particles are embedded. Indeed, the fraction of ballistic photons from the two beams reaching the HNP are expected to be modulated differently due to wavelength-dependent differences in the scattering and absorption properties of the local environment. This subtle differences can be read-out with nonlinear sensitivity providing information on the local optical properties. In fact, spectrally-resolved scattering is often analysed using photon transport equation for tissue diagnostics.[42] However this approach is valid for macroscopic propagation lengths. With the approach outlined here, one

could spectrally resolve scattering phenomena on length-scales considerably smaller than those associated with the diffusive approximation, but longer than those typical for standard microscopy thanks to the extended propagation allowed by excitation in the SWIR region.[43] We expect that this length-scale is suited to explore tissue micro-architecture for correlating, for example, the relationship between the extracellular matrix and the cancer onset in a tissue.

Conclusions

We have shown that metal-oxide particles with no prior strict morphology- or size-selection readily generates a multi-order phase-coherent response spanning from DUV to SWIR upon tunable two-color excitation at MHz repetition rate. The full response, which features several direct harmonic emissions (up to $\chi^{(5)}$) and frequency mixing signals, is well reproduced spectrally and temporally by an analytical expression derived within the perturbative development of nonlinear optics. We have also demonstrated that the response is conserved when the particles are embedded in biological media and the excitation beams are raster-scanned, two aspects essential for developing diagnostics and sensing schemes taking full advantage of the nonlinear sensitivity of the optical read-out.[44,45]

Supplementary Information

Supporting information describing the set-up, nanoparticle characterization, and further details on data analysis and modelling is available free of charge via the internet at `http://pubs.acs.org`.

Acknowledgement

References

(1) Boyd, R. W. *Nonlinear Optics*; Electronics & Electrical; Academic Press, 2003; Vol. 5; Chapter 1, p 578.

(2) Alfano, R. R.; Shapiro, S. Observation of self-phase modulation and small-scale filaments in crystals and glasses. *Physical Review Letters* **1970**, *24*, 592.

(3) Smirnova, D.; Kivshar, Y. S. Multipolar nonlinear nanophotonics. *Optica* **2016**, *3*, 1241.

(4) Reshef, O.; De Leon, I.; Alam, M. Z.; Boyd, R. W. Nonlinear optical effects in epsilon-near-zero media. *Nature Reviews Materials* **2019**, *4*, 535–551.

(5) Sain, B.; Meier, C.; Zentgraf, T. Nonlinear optics in all-dielectric nanoantennas and metasurfaces: a review. *Advanced Photonics* **2019**, *1*, 024002.

(6) Wang, Y.; Lin, C.-Y.; Nikolaenko, A.; Raghunathan, V.; Potma, E. O. Four-wave mixing microscopy of nanostructures. *Advances in optics and photonics* **2011**, *3*, 1–52.

(7) Danckwerts, M.; Novotny, L. Optical frequency mixing at coupled gold nanoparticles. *Physical Review Letters* **2007**, *98*, 026104.

(8) Masia, F.; Langbein, W.; Watson, P.; Borri, P. Resonant four-wave mixing of gold nanoparticles for three-dimensional cell microscopy. *Optics letters* **2009**, *34*, 1816–1818.

(9) Kachynski, A. V.; Kuzmin, A. N.; Nyk, M.; Roy, I.; Prasad, P. N. Zinc oxide nanocrystals for nonresonant nonlinear optical microscopy in biology and medicine. *J. Phys. Chem. C* **2008**, *112*, 10721–10724.

(10) Jung, Y.; Tong, L.; Tanaudommongkon, A.; Cheng, J.-X.; Yang, C. In vitro and in vivo nonlinear optical imaging of silicon nanowires. *Nano letters* **2009**, *9*, 2440–2444.

(11) Geissbuehler, M.; Bonacina, L.; Shcheslavskiy, V.; Bocchio, N. L.; Geissbuehler, S.; Leutenegger, M.; Marki, I.; Wolf, J. P.; Lasser, T. Nonlinear Correlation Spectroscopy (NLCS). *Nano Letters* **2012**, *12*, 1668–1672.

(12) Dai, J.; Yuan, M.-H.; Zeng, J.-H.; Dai, Q.-F.; Lan, S.; Xiao, C.; Tie, S.-L. Controllable color display induced by excitation-intensity-dependent competition between second and third harmonic generation in ZnO nanorods. *Applied Optics* **2014**, *53*, 189–194.

(13) Zhang, Y.; Manjavacas, A.; Hogan, N. J.; Zhou, L.; Ayala-Orozco, C.; Dong, L.; Day, J. K.; Nordlander, P.; Halas, N. J. Toward surface plasmon-enhanced optical parametric amplification (SPOPA) with engineered nanoparticles: a nanoscale tunable infrared source. *Nano letters* **2016**, *16*, 3373–3378.

(14) Dubreil, L.; Leroux, I.; Ledevin, M.; Schleder, C.; Lagalice, L.; Lovo, C.; Fleurisson, R.; Passemard, S.; Kilin, V.; Gerber-Lemaire, S.; Colle, M.-A.; Bonacina, L.; Rouger, K. Multi-Harmonic Imaging in the Second Near-Infrared Window of Nanoparticle-Labeled Stem Cells as Monitoring Tool in Tissue Depth. *ACS Nano* **2017**, *11*, 6672–6681.

(15) Celebrano, M.; Locatelli, A.; Ghirardini, L.; Pellegrini, G.; Biagioni, P.; Zilli, A.; Wu, X.; Grossmann, S.; Carletti, L.; De Angelis, C.; Duo, L.; Hecht, B.; Finazzi, M. Evidence of Cascaded Third-Harmonic Generation in Noncentrosymmetric Gold Nanoantennas. *Nano letters* **2019**, *19*, 7013–7020.

(16) Liu, S.; Vabishchevich, P. P.; Vaskin, A.; Reno, J. L.; Keeler, G. A.; Sinclair, M. B.;

Staude, I.; Brener, I. An all-dielectric metasurface as a broadband optical frequency mixer. *Nature communications* **2018**, *9*, 1–6.

(17) Bonacina, L.; Mugnier, Y.; Courvoisier, F.; Le Dantec, R.; Extermann, J.; Lambert, Y.; Boutou, V.; Galez, C.; Wolf, J. P. Polar Fe(IO3)3 nanocrystals as local probes for nonlinear microscopy. *Applied Physics B: Lasers and Optics* **2007**, *87*, 399–403.

(18) Kim, E.; Steinbrück, A.; Buscaglia, M. T.; Buscaglia, V.; Pertsch, T.; Grange, R. Second-Harmonic Generation of Single BaTiO3 Nanoparticles down to 22 nm Diameter. *ACS Nano* **2013**, *7*, 5343–5349.

(19) Brasselet, S.; Le FlocâĂŹh, V.; Treussart, F.; Roch, J.-F.; Zyss, J.; Botzung-Appert, E.; Ibanez, A. In situ diagnostics of the crystalline nature of single organic nanocrystals by nonlinear microscopy. *Physical review letters* **2004**, *92*, 207401.

(20) Trebino, R.; DeLong, K. W.; Fittinghoff, D. N.; Sweetser, J. N.; Krumbügel, M. A.; Richman, B. A.; Kane, D. J. Measuring ultrashort laser pulses in the time-frequency domain using frequency-resolved optical gating. *Review of Scientific Instruments* **1997**, *68*, 3277–3295.

(21) Trebino, R.; Kane, D. J. Using phase retrieval to measure the intensity and phase of ultrashort pulses: frequency-resolved optical gating. *J. Opt. Soc. Am. A* **1993**, *10*, 1101–1111.

(22) Kilin, V.; Campargue, G.; Fureraj, I.; Sakong, S.; Sabri, T.; Riporto, F.; Vieren, A.; Mugnier, Y.; Mas, C.; Staedler, D.; Collins, J. M.; Bonacina, L.; Vogel, A.; Capobianco, J. A.; Wolf, J.-P. Wavelength-Selective Nonlinear Imaging and Photo-Induced Cell Damage by Dielectric Harmonic Nanoparticles. *ACS nano* **2020**, *14*, 4087–4095.

(23) Timpu, F.; Sergeyev, A.; Hendricks, N. R.; Grange, R. Second-harmonic enhancement with Mie resonances in perovskite nanoparticles. *Acs Photonics* **2017**, *4*, 76–84.

17

(24) Timpu, F.; Sendra, J.; Renaut, C.; Lang, L.; Timofeeva, M.; Buscaglia, M. T.; Buscaglia, V.; Grange, R. Lithium niobate nanocubes as linear and nonlinear ultra-violet Mie resonators. *Acs Photonics* **2019**, *6*, 545–552.

(25) Riporto, J.; Urbain, M.; Mugnier, Y.; Multian, V.; Riporto, F.; Bredillet, K.; Beauquis, S.; Galez, C.; Monnier, V.; Chevolot, Y.; Gayvoronsky, V.; Bonacina, L.; Le Dantec, R. Second harmonic spectroscopy of ZnO, BiFeO 3 and LiNbO 3 nanocrystals. *Optical Materials Express* **2019**, *9*, 1955–1966.

(26) Joulaud, C.; Mugnier, Y.; Djanta, G.; Dubled, M.; Marty, J.-C.; Galez, C.; Wolf, J.-P.; Bonacina, L.; Le Dantec, R. Characterization of the nonlinear optical properties of nanocrystals by Hyper Rayleigh Scattering. *Journal of nanobiotechnology* **2013**, *11 Suppl 1*, S8.

(27) Le Dantec, R.; Mugnier, Y.; Djanta, G.; Bonacina, L.; Extermann, J.; Badie, L.; Joulaud, C.; Gerrmann, M.; Rytz, D.; Wolf, J. P.; Galez, C. Ensemble and individual characterization of the nonlinear optical properties of ZnO and BaTiO3 nanocrystals. *Journal of Physical Chemistry C* **2011**, *115*, 15140–15146.

(28) Wang, S.; Fu, L.; Zhang, Y.; Wang, J.; Zhang, Z. Quantitative Evaluation and Optimization of Photothermal Bubble Generation around Overheated Nanoparticles Excited by Pulsed Lasers. *J. Phys. Chem. C* **2018**, *122*, 24421–24435.

(29) Hsieh, C.-L.; Pu, Y.; Grange, R.; Psaltis, D. Second harmonic generation from nanocrystals under linearly and circularly polarized excitations. *Optics express* **2010**, *18*, 11917–11932.

(30) Bonacina, L.; Brevet, P.-F.; Finazzi, M.; Celebrano, M. Harmonic generation at the nanoscale. *Journal of Applied Physics* **2020**, *127*, 230901.

(31) Débarre, D.; Supatto, W.; Pena, A.-M.; Fabre, A.; Tordjmann, T.; Combettes, L.;

Schanne-Klein, M.-C.; Beaurepaire, E. Imaging lipid bodies in cells and tissues using third-harmonic generation microscopy. *Nature methods* **2006**, *3*, 47–53.

(32) Vuilleumier, J.; Gaulier, G.; De Matos, R.; Ortiz, D.; Menin, L.; Campargue, G.; Mas, C.; Constant, S.; Le Dantec, R.; Mugnier, Y.; Bonacina, L.; Gerber-Lemaire, S. Two-Photon-Triggered Photorelease of Caged Compounds from Multifunctional Harmonic Nanoparticles. *ACS applied materials & interfaces* **2019**, *11*, 27443–27452.

(33) Sun, X.; Ji, Z.; He, S. SHG-enhanced NIR-excited in vitro photodynamic therapy using composite nanoparticles of barium titanate and rose Bengal. *RSC advances* **2019**, *9*, 8056–8064.

(34) Malkinson, G.; Mahou, P.; Chaudan, E.; Gacoin, T.; Sonay, A. Y.; Pantazis, P.; Beaurepaire, E.; Supatto, W. Fast in vivo imaging of SHG nanoprobes with multiphoton light-sheet microscopy. *ACS Photonics* **2020**, *7*, 1036–1049.

(35) Kim, H.; Bryant, G. W.; Stranick, S. J. Superresolution four-wave mixing microscopy. *Optics express* **2012**, *20*, 6042–6051.

(36) Huttunen, M. J.; Abbas, A.; Upham, J.; Boyd, R. W. Label-free super-resolution with coherent nonlinear structured-illumination microscopy. *J. Opt. (United Kingdom)* **2017**, *19*, 85504.

(37) Extermann, J.; Bonacina, L.; Courvoisier, F.; Kiselev, D.; Mugnier, Y.; Le Dantec, R.; Galez, C.; Wolf, J.-P. Nano-FROG: Frequency resolved optical gating by a nanometric object. *Optics Express* **2008**, *16*, 10405–10411.

(38) Li, H.; Zhang, Z.; Xu, Q.; Shi, K.; Jia, Y.; Zhang, B.; Xu, Y.; Liu, Z. Characterizing ultrashort optical pulses using second-order nonlinear nanoprobes. *Applied Physics Letters* **2010**, *97*, 261108.

(39) Li, H.; Edwards, P. S.; Zhang, Z.; Zhang, B.; Xu, Y.; Gopalan, V.; Liu, Z. Characterization of the second-harmonic response of second-order nonlinear probes. *JOSA B* **2011**, *28*, 2844–2847.

(40) Accanto, N.; Nieder, J. B.; Piatkowski, L.; Castro-Lopez, M.; Pastorelli, F.; Brinks, D.; Van Hulst, N. F. Phase control of femtosecond pulses on the nanoscale using second harmonic nanoparticles. *Light: Science & Applications* **2014**, *3*, e143–e143.

(41) Mehta, N.; Yang, C.; Xu, Y.; Liu, Z. Characterization of the spatiotemporal evolution of ultrashort optical pulses using FROG holography. *Optics Express* **2014**, *22*, 11099–11106.

(42) Steelman, Z. A.; Ho, D. S.; Chu, K. K.; Wax, A. Light-scattering methods for tissue diagnosis. *Optica* **2019**, *6*, 479–489.

(43) Sordillo, L. A.; Pu, Y.; Pratavieira, S.; Budansky, Y.; Alfano, R. R. Deep optical imaging of tissue using the second and third near-infrared spectral windows. *Journal of biomedical optics* **2014**, *19*, 056004–056004.

(44) Ghirardini, L.; Baudrion, A.-L.; Monticelli, M.; Petti, D.; Biagioni, P.; Duò, L.; Pellegrini, G.; Adam, P.-M.; Finazzi, M.; Celebrano, M. Plasmon-enhanced second harmonic sensing. *The Journal of Physical Chemistry C* **2018**, *122*, 11475–11481.

(45) Mesch, M.; Metzger, B.; Hentschel, M.; Giessen, H. Nonlinear plasmonic sensing. *Nano letters* **2016**, *16*, 3155–3159.